DETERMINING ELEMENTAL CONCENTRATIONS OF NICKEL-DOPED IRON SAMPLES THROUGH THE METHOD OF LASER INDUCED BREAKDOWN SPECTROSCOPY

A THESIS IN
Physics

Presented to the Faculty of the University
of Missouri – Kansas City in partial fulfillment of
the requirements for the degree

MASTER OF SCIENCE

by
JESI CLAIRE POLARIS

B.S., The University of Tulsa, 2015

Kansas City, Missouri
2017

DETERMINING ELEMENTAL CONCENTRATIONS OF NICKEL-DOPED IRON SAMPLES THROUGH THE METHOD OF LASER INDUCED BREAKDOWN SPECTROSCOPY

Jesi Claire Polaris, Candidate for the Master of Science Degree

University of Missouri – Kansas City, 2017

ABSTRACT

Accurate information about the composition and concentration of the elements comprising a material is oftentimes of the utmost importance. Laser induced breakdown spectroscopy (LIBS) is a method for determining compositional information of materials with minimal to no sample preparation and with limited destructiveness. In this work, an optical path configuration for achieving ablation that is suitable for both LIBS and micro-LIBS is constructed. Using the optical path, LIBS spectra are taken for a series of iron samples with progressively reduced nickel-dopant concentrations in the range of 10% down to 0%. Subsequently, a spectral data analysis process is defined to enable the production of calibration curves for nickel concentrations in doped samples of iron that may be extended beyond the range studied here. The experimental setup, data acquisition, and data analysis processes in this thesis are immediately generalizable to a range of metal alloys with varying numbers of elements and relative concentrations.

APPROVAL PAGE

The faculty listed below, appointed by the dean of the college of Arts and Sciences, have examined a thesis titled "Determining Elemental Concentrations of Nickel-Doped Iron Samples through the Method of Laser Induced Breakdown Spectroscopy", presented by Jesi Claire Polaris, candidate for the Master of Science degree, and certify that in their opinion, it is worthy of acceptance.

Supervisory Committee

Paul Rulis, Ph.D., Committee Chair
Department of Physics and Astronomy

Da-Ming Zhu, Ph.D.
Department of Physics and Astronomy

Elizabeth Stoddard, Ph.D.
Department of Physics and Astronomy

TABLE OF CONTENTS

LIST OF ILLUSTRATIONS

Figure Page

LIST OF TABLES

Table Page

ACKNOWLEDGEMENTS

I would not be where I am in my education today if not for the help of others. I would very much like to thank those people who have supported me in my academic journey. First, to Dr. Jerzy Wrobel, whose research group I joined in the summer of 2016. Dr. Wrobel has since entered retirement, but has not stopped being a continuous source of knowledge and kindness. I will never forget the enjoyment and the sense of comfort in my academic endeavors I felt while working with him. It was truly a privilege. Next, to Dr. Paul Rulis, who kindly became my advisor following Dr. Wrobel's retirement. I directly attribute the completion of this thesis to the encouragement and assistance given to me by Dr. Rulis. I wholeheartedly look forward to any and all future work that I might have with him.

I would like to thank my lab partner Gabrielle Lambton for assisting me every step of the way towards completing my research. Gabrielle was always ready to be a sounding board for my thoughts. For that, I am very grateful.

I would like to thank my parents and my close friends, all of whom I consider to be family. I will be forever grateful for the support and patience they have always shown me. The unparalleled happiness I feel by sharing my life with those I love makes every challenge I face so much easier.

CHAPTER 1

INTRODUCTION

Description and Uses of LIBS

Laser induced breakdown spectroscopy (LIBS) is the method of using a high power laser to induce a plasma state in a material for the purpose of spectroscopy. LIBS has become extremely diverse in its applications over the last few decades, finding use in such areas as geophysics, archeometry, nutrition studies, the alcoholic beverage industry, military applications, medicine, additive manufacturing, and waste management[1–4]. The popularity of LIBS is primarily a result of its procedural simplicity. If the laser system is functioning as intended, there typically are only three factors that can complicate the procedure for doing LIBS; the laser beam must be focused enough to ablate the surface of the sample, the spectrometer must be in position to view the emissions of plasma as it cools[5], and the spectrometer must view the plasma plume at the correct time after ablation[5,6].

There is minimal to no sample preparation necessary for LIBS, and it is portable[7]. This is extremely convenient for researchers who want to study materials in environments that might be dangerous or impossible for humans to reach, such as on the surface of Mars or in highly radiative environments[2]. The lack of a sample preparation requirement means that LIBS can be employed from a distance, even up to several meters[2]. Illuminating this fact, LIBS has been used in military applications to detect explosives without ever having to expose personnel or expensive hardware to danger[2]. Not having to do any sample preparation means that LIBS is most often free of impurity chemicals, which has broad and important implications in the food industry and nutrition studies[4,8–11]. LIBS is minimally

invasive because it creates an ablation crater that is on the order of only tens of microns in diameter and depth[12]. The relative noninvasiveness of LIBS makes it a convenient tool in the field of medicine when analysis of live specimens is necessary, or when there are only samples of very small size. LIBS is fast, giving spectroscopic information instantly. This aspect of LIBS has been exploited by the incorporation of conveyer belts to do sample testing in bulk.[13,14] Cama-Moncunill et al. used LIBS at-line to analyze infant formula in the factory, and Sorrentino et al. used LIBS to analyze scrap metal, both studies incorporating conveyer belts.

LIBS has multi-element analytic capabilities[15] and can be done regardless of a sample's physical state (solid, liquid, or gas), meaning that it is well-suited for determining elemental concentrations in materials[7,16,17]. In order to determine the concentrations of the elements comprising a sample, a calibration curve needs to be developed. The development of such curves is an active area of research, and also the purpose of this thesis.

Purpose and Motivation of Project

Oftentimes in industry, especially in fields relating to materials development, it is crucial to know the exact elemental composition and the concentrations thereof of the materials that are involved. For example, the concentration of cobalt in steel plays an important role in the magnetic and thermal properties of steel[18]. If a particular form of steel is being developed to be used in a specific magnetic or thermal environment, it is essential to know the concentration of cobalt in the material. A common strategy for determining the elemental composition of a material is through spectroscopic methods such as LIBS. Elemental spectral information can be found in databases such as the NIST: Atomic Spectra Database[19]. If an accurate LIBS spectrum of the material is available, one could reference

the spectral line database to determine its elemental composition. The process of doing so involves matching emission lines from the spectrum to those in the database. However, this process will only give information about which elements are present in the material; information on their respective concentrations is not obvious but depending on the application it may be crucial information to have.

Previous Work at UMKC

Experimentation with laser ablation, as well as laser ablation spectroscopy, in the UMKC Department of Physics and Astronomy has been proceeding for several years now. Two particular activities were essential for creating a store of the optical equipment necessary for my research. The first activity was the creation of ZnO and SnO_2 thin-films via pulsed laser deposition in vacuum and the second activity was the formation of nanoparticles via the ablation of aluminum samples in water, and germanium samples in both water and ethanol[20]. Spectra of steel samples have been collected. The purpose of which was to compare spectra from a material with known multi-element composition to data in the NIST spectral line database. This comparison verified that observed compositions could accurately be determined with the LIBS system in the lab. Spectra from other random metal samples have been taken and compared to one another via emission line matching to see which emissions were common amongst them. This allowed the formation of reference data about their shared elemental compositions. Preliminary work relating the spectral line intensities of a material to the concentrations of the elements comprising it was the precursor to my research project[21]. The work done to-date on that topic has not produced definitive results. Therefore, finding a definitive relationship between spectral line intensity and concentration was the purpose of my project.

Outline of Thesis

The purpose of this research was to use laser induced breakdown spectroscopy to accurately determine the concentrations of nickel in doped samples of iron. An experimental method and data analysis process was developed for the production of a calibration curve that displays the relationship between spectral emissions of nickel and its concentration within the doped sample. In the following chapters of this thesis, a description in full detail is given about the process that led to the creation of the calibration curve. All research methods employed in this work are presented in Chapter 2. These methods involve the choice of samples, process for gathering data, and designs for instrumentation configurations. Spectral results are rigorously analyzed and discussed in Chapter 3. Through this analysis, a calibration curve for nickel concentrations in doped samples of iron is produced. Suggestions are then given for future research projects that use this work as a precursor. A summary of this research concludes the thesis in Chapter 4.

CHAPTER 2

RESEARCH METHODS

Excimer Laser

I used a Coherent COMPex Pro 351nm excimer laser to do all of my research on laser induced breakdown spectroscopy. This laser uses fluorine as its halogen laser gas, and helium as its inert gas. The gas mixture in the laser tube that acts as the active medium is 5% F_2 to He. The UV emissions are pulsed with each pulse lasting 20ns and the pulses occurring at a frequency of 1Hz. Typical radiation energy for this laser is 300mJ. It is possible to modify the radiation wavelength from 351nm to 308nm, 148nm, or 193nm through an exchange of gases (XeCl, KrF, or ArK respectively), but this was never done in my research. Figure 1 shows an image of the excimer laser that I used to conduct this experiment.

The beam profile of a laser emission describes the physical distribution of energy across the face of the beam. A common beam profile for devices such as laser pointers is Gaussian, with the bulk of the energy existing in the center of the cross-section, and falling off near the edges. Another, less common, profile is referred to as flat-top. Unsurprisingly, this profile describes a cross-sectional energy distribution that is constant across its width.

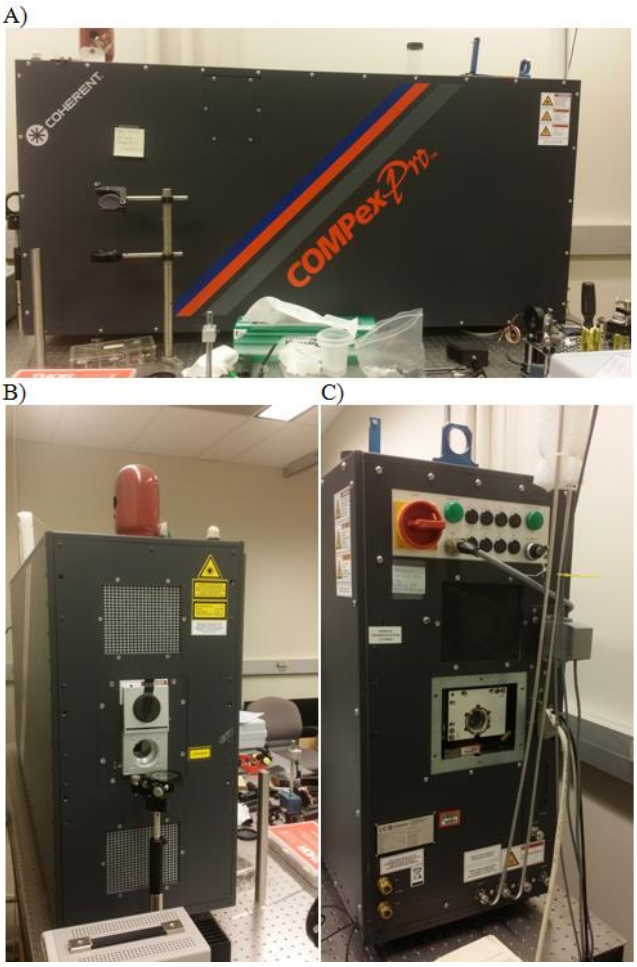

Figure 1. Coherent laser - (A) Front; (B) Side; (C) Rear

The beam profile of the emissions of the Coherent laser can be controlled by making modifications to the internal optics of the laser's resonator. The laser was initially off-line when I began my research project, and during the time that work was being done to bring the laser back to normal operation the resonator optics were set to their "stable" configuration, resulting in a Gaussian beam profile. It was later determined that the Gaussian profile was not radially circular; rather, it was rectangular. The beam energy did behave as a Gaussian, normally distributed as it falls off towards the edges of the beam, but the perimeter defining the edge of the beam itself was not circular.

There was no reason to believe that that would cause any problems at the beginning of my project, so the beam profile was left as-is. It was assumed that having a Gaussian beam profile would be preferable to flat-top profile because it is typically easier to focus a beam with a Gaussian profile than it is to focus one that is flat-top. A more focused beam will have a smaller spot size, making a Gaussian beam profile more suitable for microLIBS (LIBS done on micron-scale particles).

Once the laser was operational, I designed an optical path for the purpose of achieving ablation. I immediately noticed that multiple ablation spots appeared at the end of my path. This issue lingered for quite some time while different path configurations were tested. It was eventually discovered that the Gaussian beam was constructed by an overlapping of emission modes. An image of the multimodal beam was taken with a beam profiler and is shows in Figure 2.

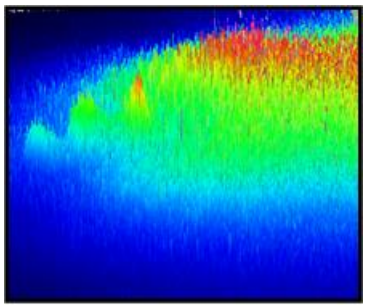

Figure 2. Multimodal beam profile

When the multimodal beam was focused by a convex lens, multiple beams were produced. This effect is shown in Figure 2. In this figure, the peaks emerging from the blue/black background represent laser energy density. The color represents laser intensity with red being the brightest. This image is a slightly rotated view of a normally incident beam profile taken with a beam profiler, with the rotation being into the page. Each peak in Figure 2 corresponds to separate ablation spot. This is further demonstrated in Figure 3.

It was assumed that adjustments made to the internal resonator optics would cause the spots to be merged into one. However, this was not the case.

It is inherent to the nature of the multimodal Gaussian beam profile that it cannot be limitlessly resolved into a single spot. While in their "stable" configuration, there are no positions of the internal resonator optics that can resolve the multiple ablation spots into one. Below in Figures 3, an image of multiple ablations of a highly focused multimodal Gaussian beam profile is shown. As can be seen in the image, there are at least five (possibly more) separate spots comprising each ablation area. The red lines appearing on one of the ablated regions distinguishes the multiple spots in that region.

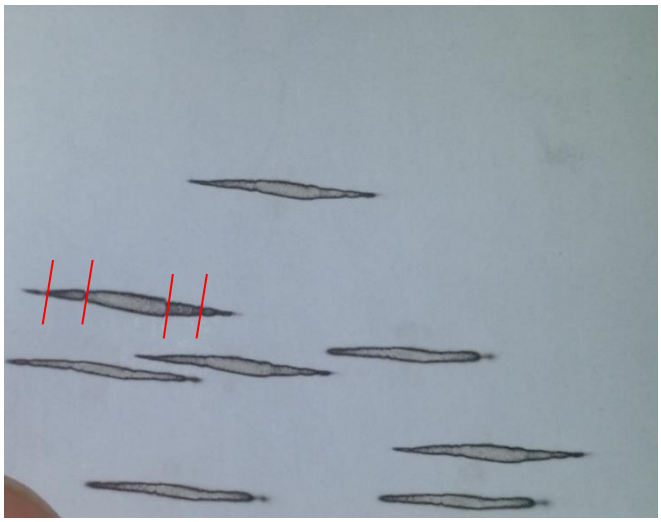

Figure 3. Multiple spots resulting from focusing

Figure 4. Stable resonator beam profiles - (A) Least aligned; (B) Better aligned; (C) Most aligned.

Figure 4 shows the results of my attempts to align the internal optics of the resonator in its stable configuration. The beam spots are shown on thermal paper, and are approximately 1cm in length. Each darkened area is a region where the laser has struck the thermal paper. Fringes exist in each of these areas. Even while in its most aligned state, it was impossible to resolve the beam into a single spot.

The solution to the unresolved nature of the Gaussian beam profile under focusing was to switch to a different beam profile. The internal optics of the laser was reconfigured for its unstable resonator configuration. This configuration produces a flat-top beam profile. Figure 5 shows the success of switching to the flat-top beam profile.

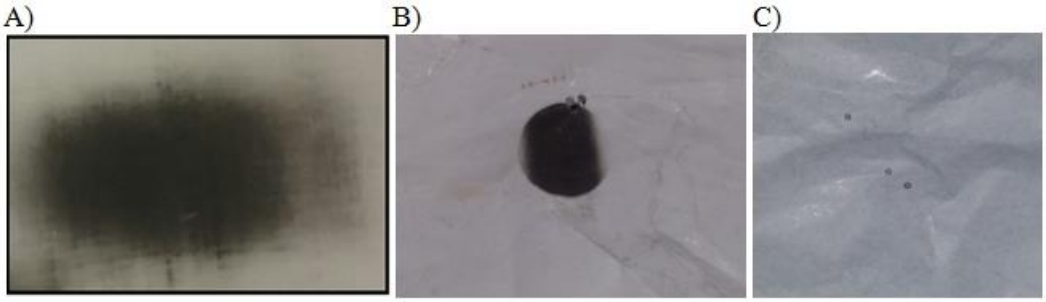

Figure 5. Flat-top beam profile - (A) Unfocused; (B) Partially focused; (C) Fully focused

Similar to Figure 4, the images appearing in Figure 5 are of thermal paper used for laser beam alignment. Figure 5 (A) shows what the flat-top beam profile looks like while unfocused, directly after being emitted from the laser. The beam profile has a diameter of ~4cm when unfocused. Figure 5 (B) is of the beam profile after being focused through a mid-power convex lens. The scale at this point is comparable to the ablation spots shown in Figure 4, approximately 1cm. Figure 5 (C) is of the beam profile after being fully focused through the main objective used for ablation. The thermal paper was not placed exactly at the focal point of the lens so the ablation spots in this image are much larger than their minimum size. They are approximately 1mm in this image.

Optics and Visualization

All tested configurations of the optical path were designed with the potential of future application to microLIBS in mind. Another graduate student in the laboratory, Gabrielle Lambton, was researching the topic of microLIBS. Whether or not the path worked for well for microLIBS was irrelevant to the current research because there was no meaningful upper bound on the amount of the sample to ablate with each pulse. Nevertheless, the configurations described below—which are also useful for microLIBS—were the ones used in this research. Therefore, they deserve to be discussed.

In many applications, especially those related to additive manufacturing, it is crucial to be able to aim the laser onto a specific region of the sample, hence research interests in microLIBS[21]. In order to do that, it is necessary to be able to visualize precisely where ablation was occurring on the sample. The solution was to incorporate a camera into the optical path so that it would be possible to view the sample on a video screen. There were two configurations used that served separate purposes. The first configuration described below is more suitable for microLIBS and the second is more suitable for general sample viewing.

To do microLIBS, one must use a computer to highlight regions of interest on the sample. Thus, a camera capable of interfacing with a computer was necessary. This was accomplished using Thorlab's Thorcam software. With this software, it is possible to view where ablation is occurring on the sample. The following discussion describes the optical path used for sample visualization, as well as the procedure for aiming the laser.

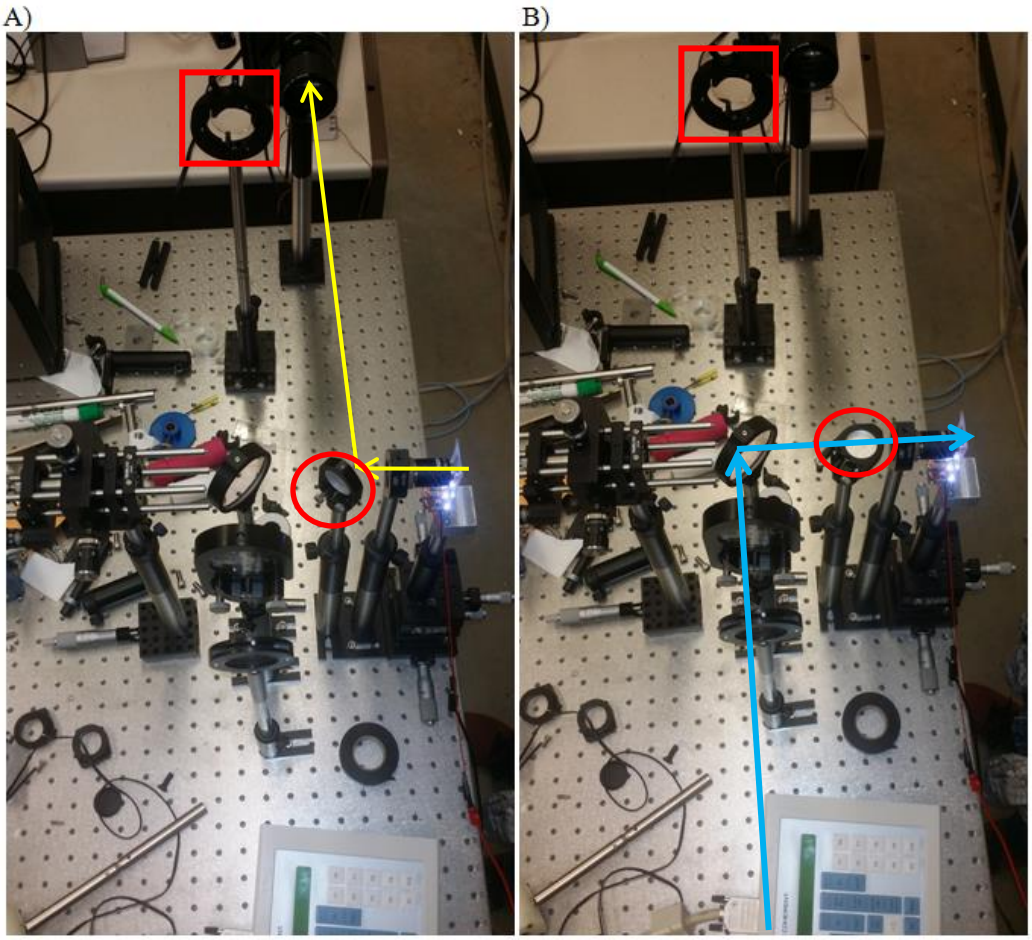

Figure 6. Optical path - (A) Visualization mode; (B) Ablation mode

Figure 6 (A) and (B) show how the optical path was designed to view the sample. In Figure 6 (A), the circled flip mirror is in its visualization mode. Light from the illuminated sample holder reflects off of the sample into the main objective. The image of the sample is then reflected off of the flip mirror, through a focusing lens (squared and out of position in the figure), and into the camera interfacing with the computer. Once the computer has the image, the aiming process follows the description given in Figure 7 (A) - (D).

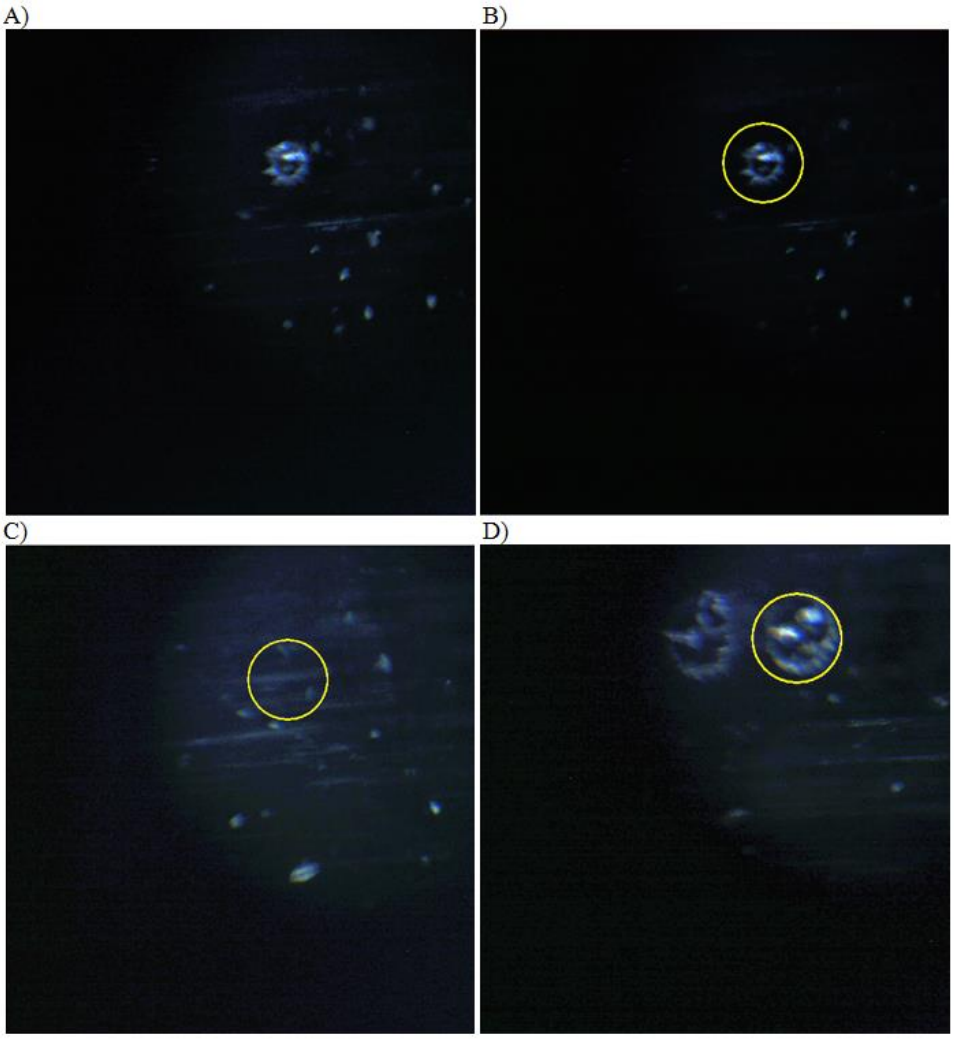

Figure 7. Aiming process - (A) Ablate without aiming; (B) Highlight resultant crater; (C) Adjust translation stage; (D) Ablate in highlighted region

The flip mirror shown in Figure 6 (B) must first be flipped down into ablation mode so that the laser pulse can reach the sample. Then a series of pulses strong enough to create a visible crater must be shot onto the sample (Figure 7 (A)). An image of the ablation crater will appear once the mirror is flipped back up. Then, using the Thorlab's Thorcam software, the crater is highlighted on the screen so that the location on the screen that correlates with the ablation site is known (Figure 7 (B)). Intuitive adjustments are then made to the micrometers on the translation stage holding the sample until the region of interest is within

the highlighted region. Figure 7 (C) shows a region of interest that is encompassed by the targeting circle. Figure 7 (D) shows the success of this aiming process. A new crater is within the highlighted region. The other crater appearing in Figure 7 (D) is from a prior ablation and irrelevant to the aiming process just described.

The size of a crater formed by ablation is dependent on the degree to which the laser beam is focused. To test if the craters are of the appropriate size, they must be viewed under a microscope. Figure 8 (A) - (B) shows images of craters created by partially focused and fully focused beams, the latter being of an appropriate size for microLIBS.

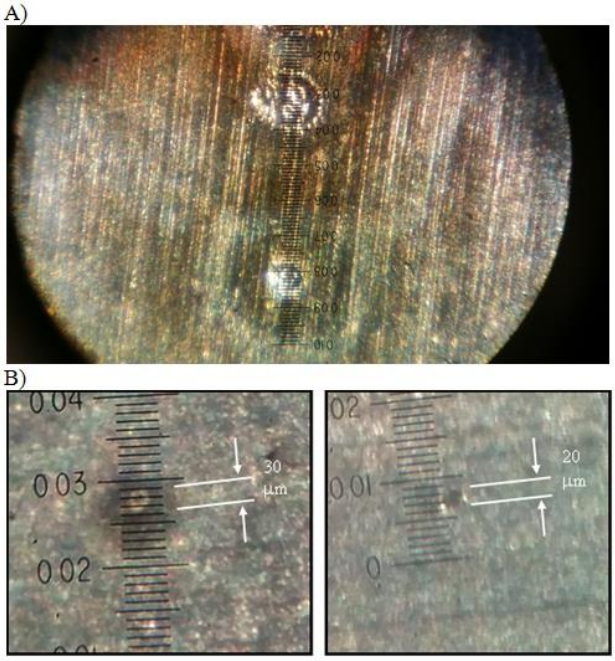

Figure 8. Ablation craters - (A) Partially focused, (B) Fully focused

Both the limits of visualization and the degree to which the laser beam can be focused had a lower bound of approximately 30 microns. The vials appearing in Figure 9 contain 304 steel particles of ~30 micron diameter. Figure 10 shows verification of this under a microscope.

Figure 9. Vials of powdered 304 steel

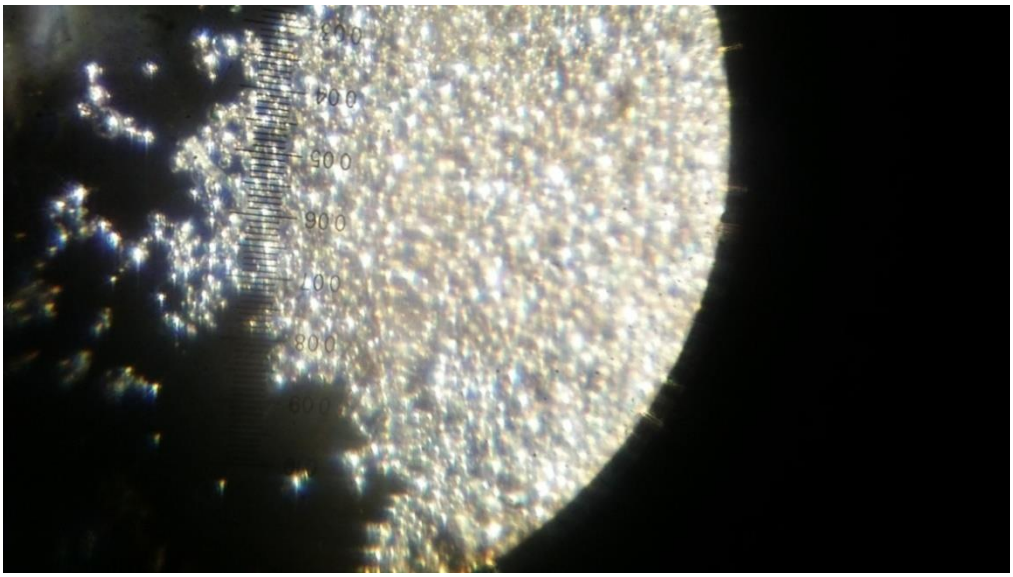

Figure 10. Powdered 304 steel under microscope

A small amount of sample preparation was needed to ablate the powdered 304 steel sample. In order to ablate these particles, they needed to first be soaked in isopropanol while resting on a microscope slide. Once enough time had passed for the alcohol to evaporate, the powder had adhered to the microscope slide. The slide shown in Figure 11 was then inserted into the illuminated sample holder shown in Figure 6. When the optical path was set to visualization mode, the image shown in Figure 12 was visible on the

computer monitor. As demonstrated by Figure 12 (B), the preceding visualization and aiming process works on the micrometer scale.

Figure 11. Prepared powdered 304 steel

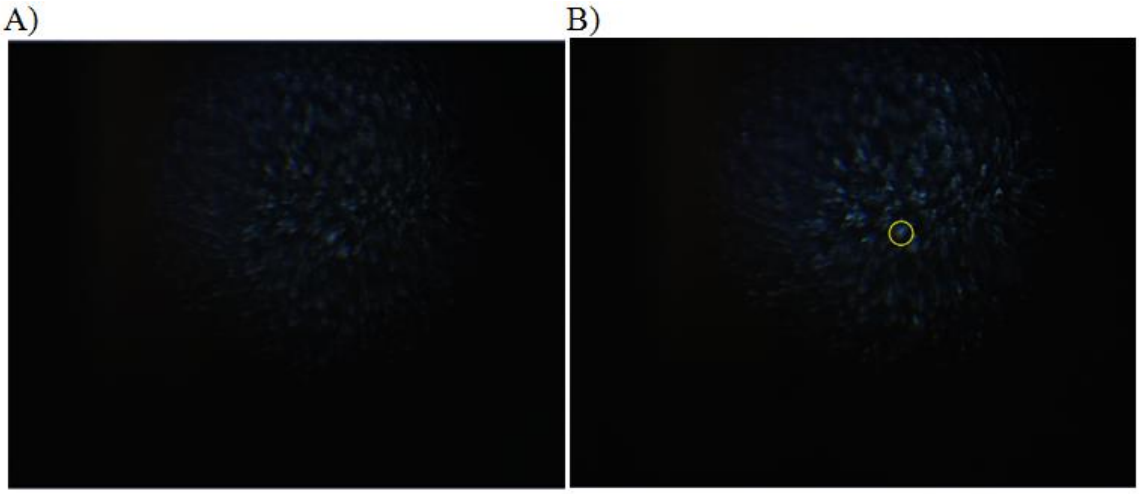

Figure 12. Powdered 304 steel visualized

The present research did not have microLIBS as a goal. Therefore, micron scale visualization was not a pre-requisite for the data collection process used for this thesis. The

next configuration is exactly the same as the one just described with the exception that an older camera that could not interface with the computer was used. The practical reason for that decision was that the data was to be collected from a bulk sample that did not require targeting of any specific regions of the material. As shown in Figure 13 through Figure 15, interfacing this camera with a CRT TV allowed one to see with the naked eye that the samples were being successfully ablated from the live video feed. With the older camera, there was no need to manage any visualization software which led to a simpler and more rapid data gathering process.

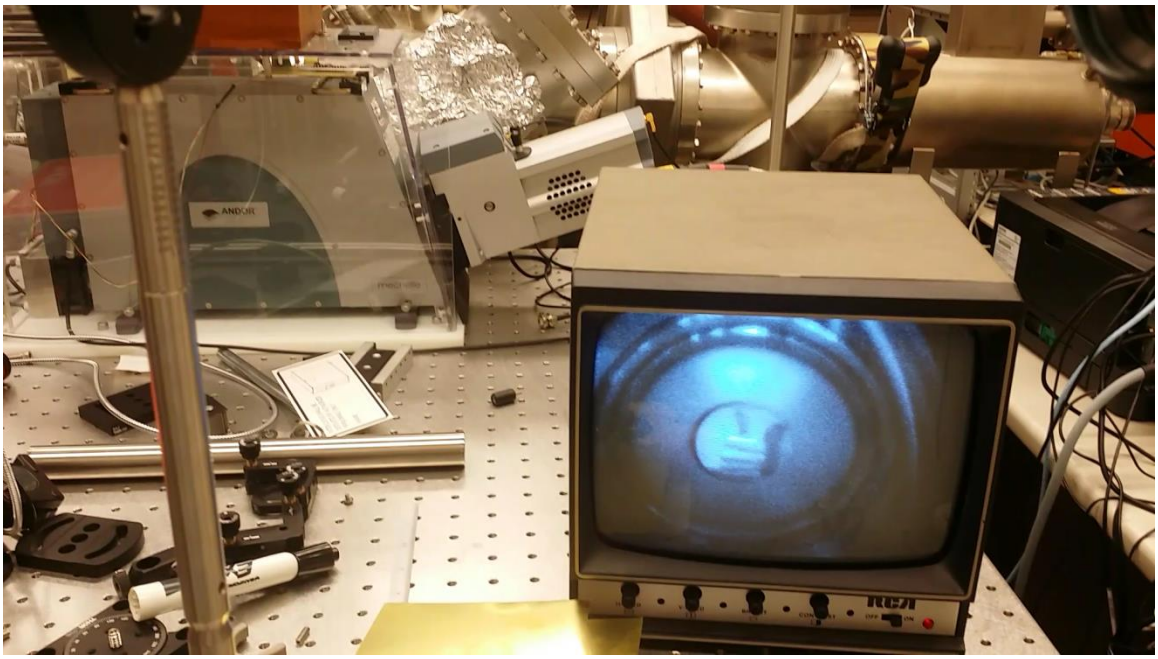

Figure 13. Visualization on the CRT

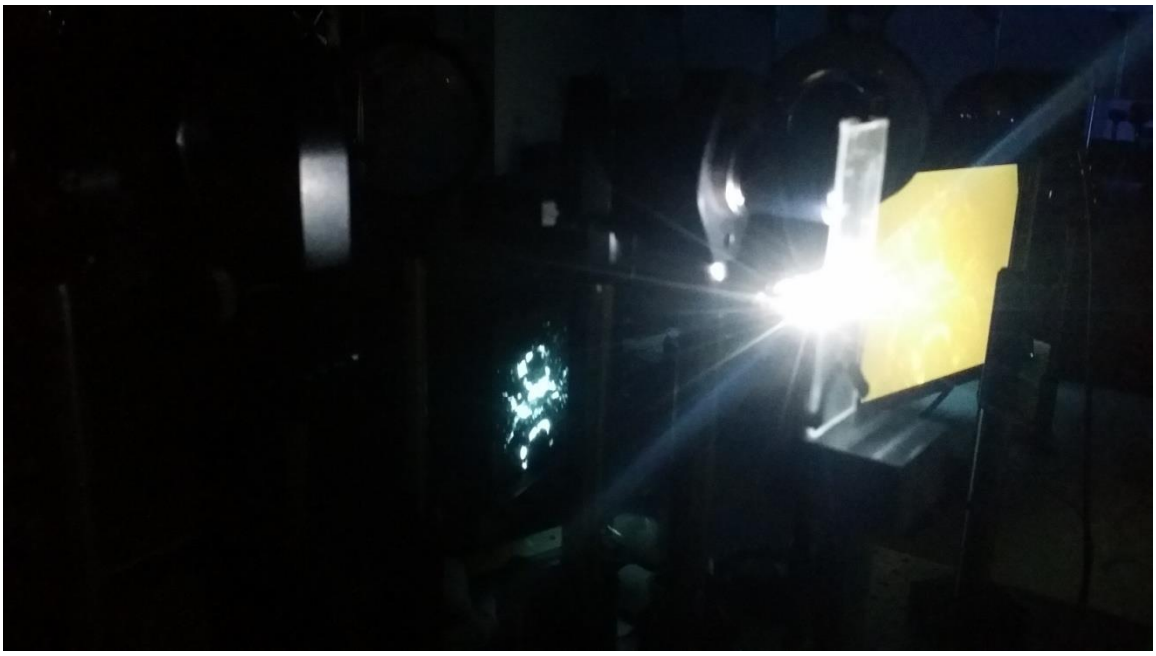

Figure 14. Visualization on CRT - with sample

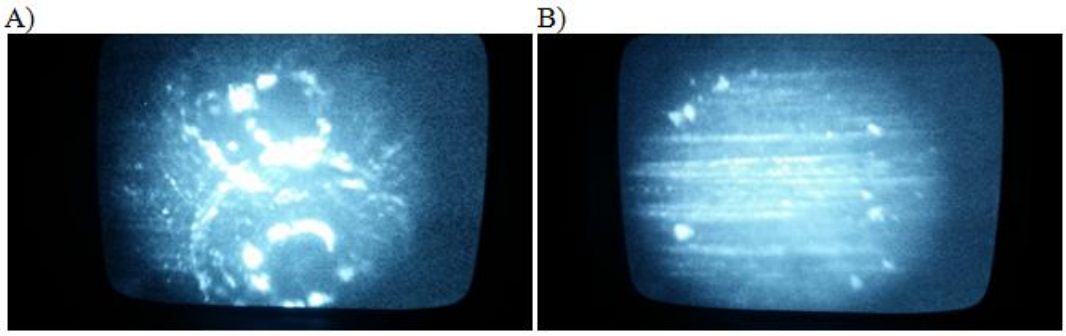

Figure 15. Visualization on CRT (another view) - (A) Ablated, (B) Un-ablated

The discussion thus far has focused solely on the optical elements relevant to visualization. The remaining elements in the configuration are shown in Figure 16 and Figure 17. The configuration shown in those images was used to collect all of the data presented in this thesis. The elements appearing in those figures are circled and numbered. A list of the elements with their corresponding numbers, given in order of incidence, follows below Figures 16 and Figure 17 and is shown in Table 1.

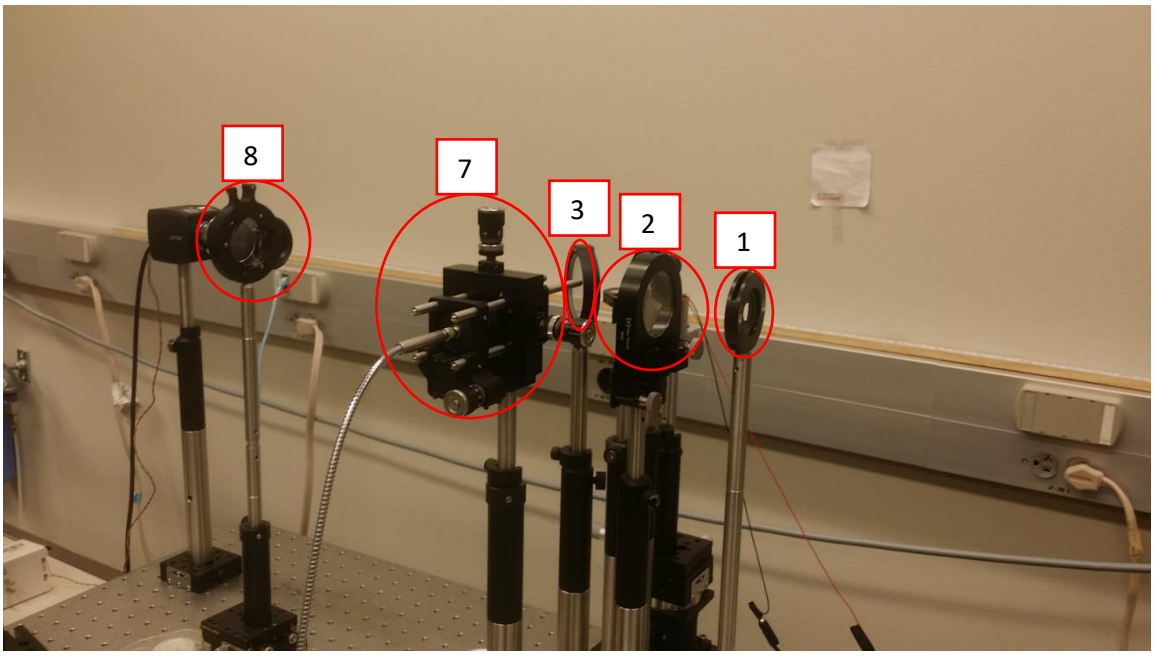

Figure 16. Configuration for data collection

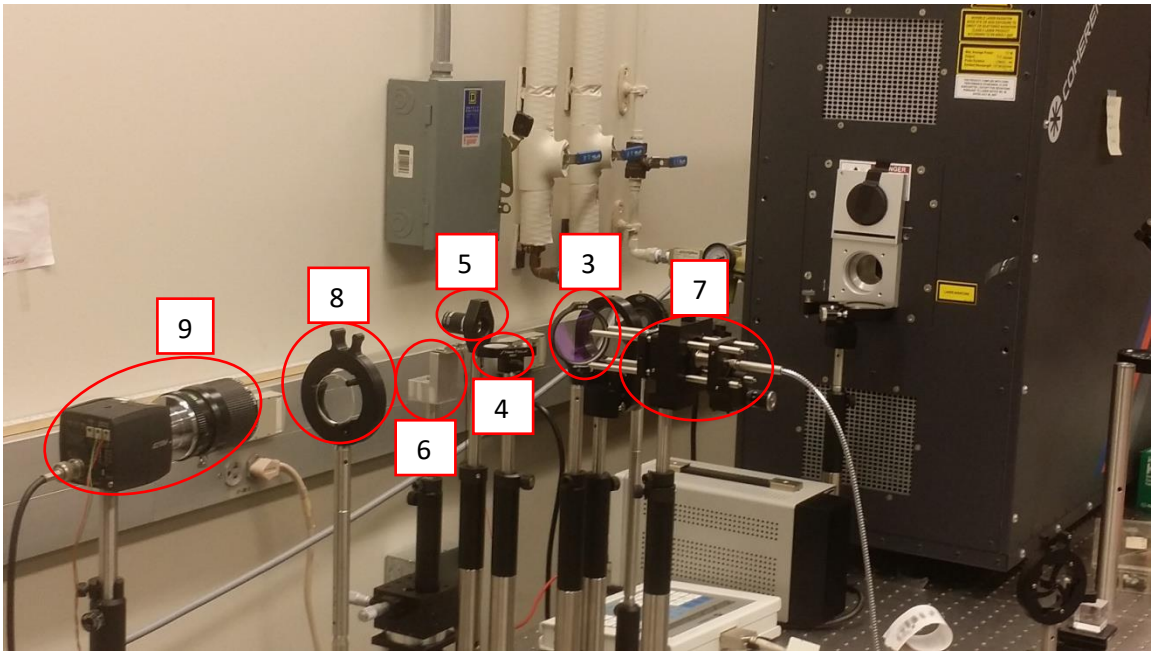

Figure 17. Configuration for data collection (another view)

Table 1. Elements in optical configuration for data collection

Order of incidence		Optical Device
1.		Aperture
2.		Mid-power convex lens
3.		UV-protected dielectric mirror
4.		Flip-mirror
5.		High-power main objective lens
6.		Sample holder (unilluminated)
7.		Mechelle 5000 echelle spectrograph fiber optic with host chassis
For sample visualization	8.	Focusing lens for sample visualization
	9.	Camera interfacing with CRT

The laser beam leaves the laser (appearing on the right side of Figure 17) and first encounters the aperture. The aperture permits only a small region of the beam profile to pass through. The smaller resultant beam is easier to focus when ablating. The beam travels through a focusing lens and then reflects off of a UV protected dielectric mirror. The mirror is mostly transparent to the visible portion of the electromagnetic spectrum, but it is reflective in the ultra-violet range (10nm – 400nm). The beam then passes over a flip-mirror (whose sole purpose is for visualization when not ablating) and into the main objective. The main objective lens has a high power of magnification and a working distance of only 1mm. Ablation occurs on the sample and the plasma plume that is created emits light. Light from the radiating plume of sample travels back through the main objective, over the flip-mirror, and through the dielectric mirror. The radiation from the plume is mostly in the 400nm – 750nm range. The light resides within the visible portion of the spectrum, allowing it to pass through the dielectric mirror and into the fiber optic

cable of the spectrometer. The spectrometer sends spectral data to the computer to be analyzed, finalizing the LIBS process.

Information about Samples

The samples that were selected for the present study are shown below in Figure 18. They were bulk iron-nickel samples with nickel content ranging from 0% to 10%, with the nickel assumed to be distributed evenly throughout the samples. The goal of the present research was to show that a relationship exists between the relative magnitudes of the emission lines of nickel and its concentration in each sample.

It should be noted that all elements have different ablation thresholds. The ablation threshold of an element is a metric that describes how easily the material ablates, and in turn how well it gives off emission spectra. For example, nickel has a much higher ablation threshold than iron. Nickel was selected because an instrumentation design and spectral analysis process that is capable of discerning the presence of nickel at low concentrations will certainly also work for materials with lower ablation thresholds.

There are of course materials with higher ablation thresholds than nickel. Tin is an example of such a material. Based on previous experiments at UMKC involving the ablation of tin, the likelihood that a spectrum could be obtained with tin emissions that were pronounced enough to do analysis on was expected to be very low.

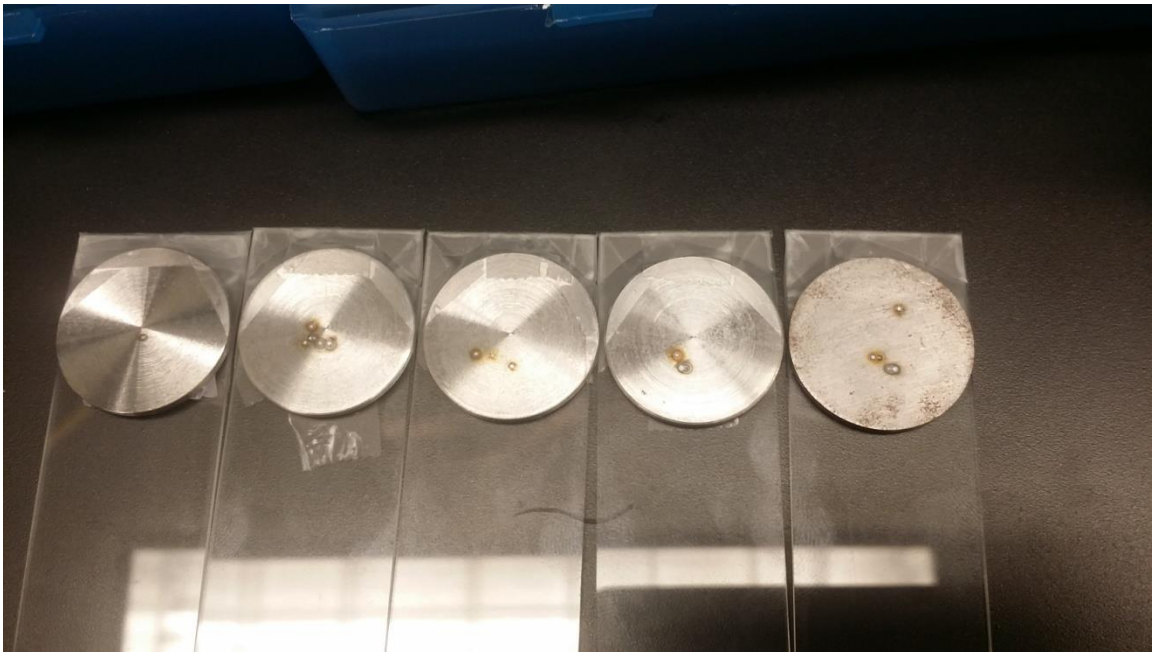

Figure 18. Fe and FeNi Samples - From right to left, Ni concentrations are 0%, 1%, 2%, 5%, and 10%

Gathering Data

There were numerous configurations of optics tested for the purpose of obtaining the best data possible. Once a suitable configuration had been found, it was used to collect all of the data used in the present research. A discussion of the optical configuration used appears in the Optics and Visualization section of this thesis, specifically shown in Figure 16 and Figure 17. All data was collected with the sample holder illuminated, the incandescent desk lamp turned on, and the overhead room lights turned off (Figure 19).

The data collection process was simple and it was the same for each sample. Beginning with a pure un-doped iron sample, the laser potential was set to 23kV and 5 spectra were obtained, each resulting from a single-pulse emission. A typical Fe spectrum is shown in Figure 21. This process was repeated with the laser potential set to 25kV and then again at 27kV. Along with the spectra, the pixel data from the spectrometer's CCD was also saved. The pixel data was not used in any quantifiable way, rather it simply served

to visually verify that the CCD was being properly illuminated by the plume of sample. A typical image of pixel data is shown in Figure 22.

Figure 19. State of the lighting environment in the room during data acquisition

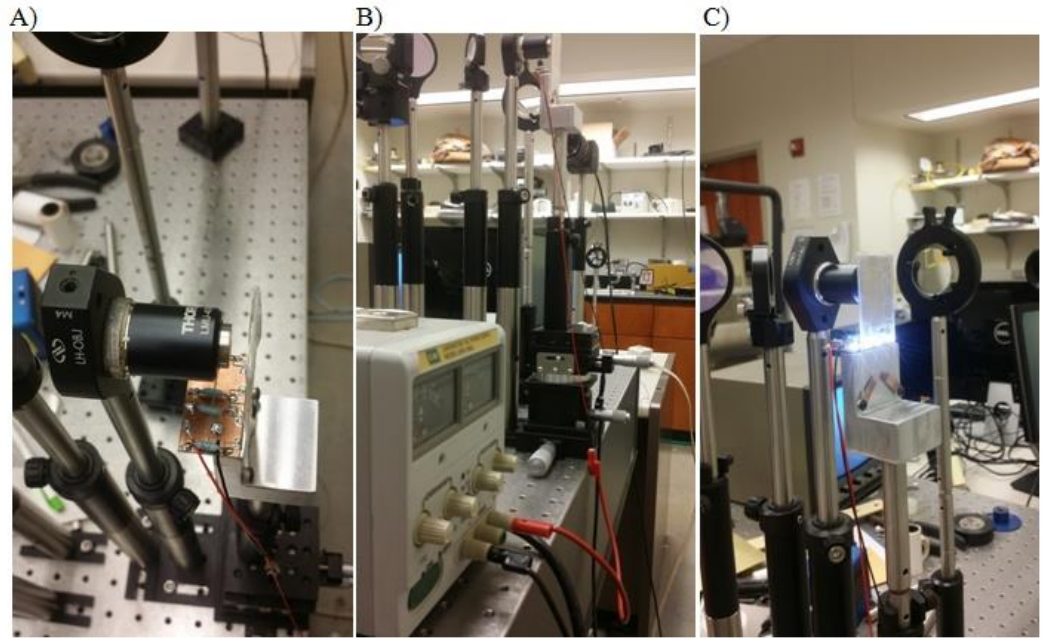

Figure 20. Sample holder - (A) Not illuminated; (B) Power source; (C) Illuminated

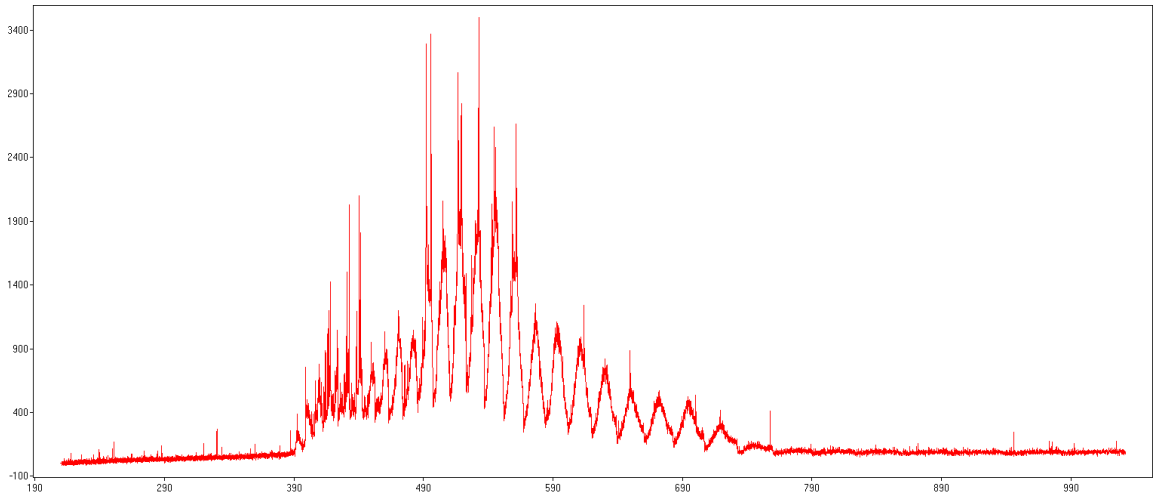

Figure 21. A typical Fe spectrum

Figure 22. A typical illuminated Echelle spectrometer CCD

That process was repeated for each of the nickel doped samples making sure to keep all variables (such as the distance between the main objective and sample) as constant as possible. Once all of the spectral data had been collected, data analysis could begin. The analysis process and the results are discussed in the following chapter of this thesis.

CHAPTER 3

RESULTS and DISCUSSION

Spectral Results and Analysis

The spectral data that were obtained following the procedures given in Chapter 2 were saved as tab-delimited ASCII files. The data was imported into a program called Spectrum Analyzer 1.7[22]. This software references NIST's atomic spectra database and allows for the identification of emission lines. Table 2, shown below, contains an example subset of the NIST database. The information contained in the NIST database that is relevant to this work is shown in the columns of Table 2 titled *Spectrum*, *Observed Wavelength Air (nm)*, and *Rel. Int.* The spectrum column is the name of the element to which the emission line belongs. The observed wavelength column gives the wavelength of the emission as measured in air. The relative intensity acts more as a qualifier for how pronounced the emission line is. The relative intensity values are from cited papers, but NIST does not give any information on the source of the values. In general, the rule when considering the relative intensity of an emission line is that lower values indicate a smaller probability that the emission line is what is actually being measured, and higher values indicate the opposite. If a given emission line has no value in its relative intensity column then the line is theoretical and it still needs to be verified by experiment.

Table 2. NIST Spectral Lines

Spectrum	Observed Wavelength Air (nm)	Ritz Wavelength Air (nm)	Rel. Int.	Aki S^-1	Acc.		Ek (cm-1)	Conf.
Th I	400.00239	400.002376	32			13847.77037	38840.5553	6d3.(4F).7s
Mn II	400.0035	400.0022	20h			62587.547	87580.34	3d5.(2D).4s
Th I	400.00413	400.004177	53			15490.077832	40482.7503	5f.6d.7s2
Ti I	400.00430	400.00442	12			16875.124	41867.7812	3d2.(3F).4s.
B III	400.007	400.017	136			1842812.7	1867804.6	1s.2s.(3S).4

W II	400.00819	400.00812	4			28377.585	53370.011	
Pr II	400.017	400.017+	620c	1.15e+07	B	1649.01	26640.86	4f3.(4I*<11/
Pr III	400.020		200					
Fe I	400.0252	400.025248	457bl	2.2e+06	E	26339.696	51331.052	3d6.(5D).4s.
Th I	400.028093	400.028091	1400			10414.13700	35405.3154	5f.6d.7s2
Th I	400.044538	400.044534	180			5563.141519	30553.29269	6d3.(4F).7s
Dy II	400.045	400.0450+	8000	2.54e+07		828.314	25818.435	4f10.(5I<8>)
Fe I	400.04570	400.045722	1480	1.01e+06	C+	24118.819	49108.896	3d6.4s2
Nd II	400.0493	400.0490+	410	7.5e+06	B+	1650.205	26640.080	4f4.(5I).6s
Xe II	400.055	400.053+	5h			114913.98	139903.63	5p4.(1D<2>).

Spectrum	Lower Level |Term	J	Conf.	Upper Level Term	J	TP Ref.	Line Ref.
Th I	| 3F	2		*	1		L5951
Mn II	| d 3D	3	3d5.(a 2G).4p	u 3F*	4		L562
Th I	| 3G*	5			5		L5951
Ti I	| z 5F*	2	3d2.4s.(4F).4d	3G	3		L10989
B III	| 4D	1/2,3/2,5/2,7/2	1s.2s.(3S).5f	4F*	3/2,5/2,7/2,9/2	L12547	
	|						
W II	|	11/2			9/2		L11762
Pr II	| (11/2,1/2)*	6			5	T8137	L3475
Pr III	|						L2466
Fe I	| z 5D*	2	3d6.(5D).4s (6D).4d	e 7F	2	T2578n	L11631
Th I	| 1G*	4			3		L5951
	|						
Th I	| 5F	1		*	2		L5951
Dy II	| (8,1/2)	15/2	4f10.(5I).6p	*	17/2	T7148	L3475
Fe I	| b 3G	4	3d7.(2G).4p	w 3F*	4	T5720	L11631
Nd II	| 4I	9/2	4f4.(5I).6p	6H*	7/2	T7685	L3260,L3475
Xe II	| 2[4]	7/2	5p4.(3P<2>).4f	2[5]*	9/2		L6925

To better understand the process of relating a collected spectrum to the data from NIST, consider attempting to label an emission line appearing around 532.4nm that is located in a spectrum taken from a sample known to contain solely iron at 99% purity. There might be three possible lines to choose from in a range of +/- 0.05nm around where the peak exists in the spectrum. The first is Mo with a relative intensity of 20, the second

is Fe with a relative intensity of 150, and the last is Ti with an absent relative intensity. The correct emission to choose in this case would be Fe. In this example, the Fe line has a higher relative intensity than the Mo line. Therefore, there have been at least two spectra from cited publications with one containing the Fe line and the other containing the Mo line. The higher relative intensity of the Fe line means that that line is more pronounced in its spectrum than the Mo line is in the other. Further, the sample was known to contain iron at 99% purity. It is possible that there is Mo in the 99% pure Fe sample, but because the relative intensity of the Mo line is lower than the Fe line it is safe to assume that even if there was Mo known to be in the sample, it is more likely that this line belongs to Fe. The Ti line is the worst option to choose because the line associated with it in the NIST database is only a theoretical prediction and it has not even been observed yet.

The mechanism by which elemental concentrations in a sample may be obtained using LIBS is to relate changes in emission line intensities of the elements to changes in their concentration in a sample. Nickel-doped iron samples with concentrations of nickel ranging from 0% to 10% were used in the present research. The first step to achieve the goal of determining nickel concentration was to determine which lines in the spectra belonged to nickel. As mentioned before, nickel has a higher ablation threshold than iron, making the emission lines from nickel much less pronounced than those from iron in the collected spectra. The precise location of the nickel lines in the spectra was not clear so a special method was developed to locate them.

The solution to the problem was to calibrate the data by comparing emission counts across the entirety of each spectrum in all of the nickel-doped samples against the emission counts of the pure iron sample. An Excel spreadsheet was created for each sample at each

voltage, yielding fifteen spreadsheets total (three voltages for each of the five samples). As stated in the "Gathering Data" section of the Chapter 2, five spectra were obtained for each sample at a given voltage. In the calibration process, the first step was to normalize every emission line in the spectra because comparing emission counts between spectra is pointless without normalization. This was done by taking a sum of the counts for all wavelengths in the spectra, and dividing the individual emission lines by this value. Next, a "typical" normalized spectrum was created for each sample by averaging the normalized values of emission. An example of such a normalized spectrum is given in Figure 23.

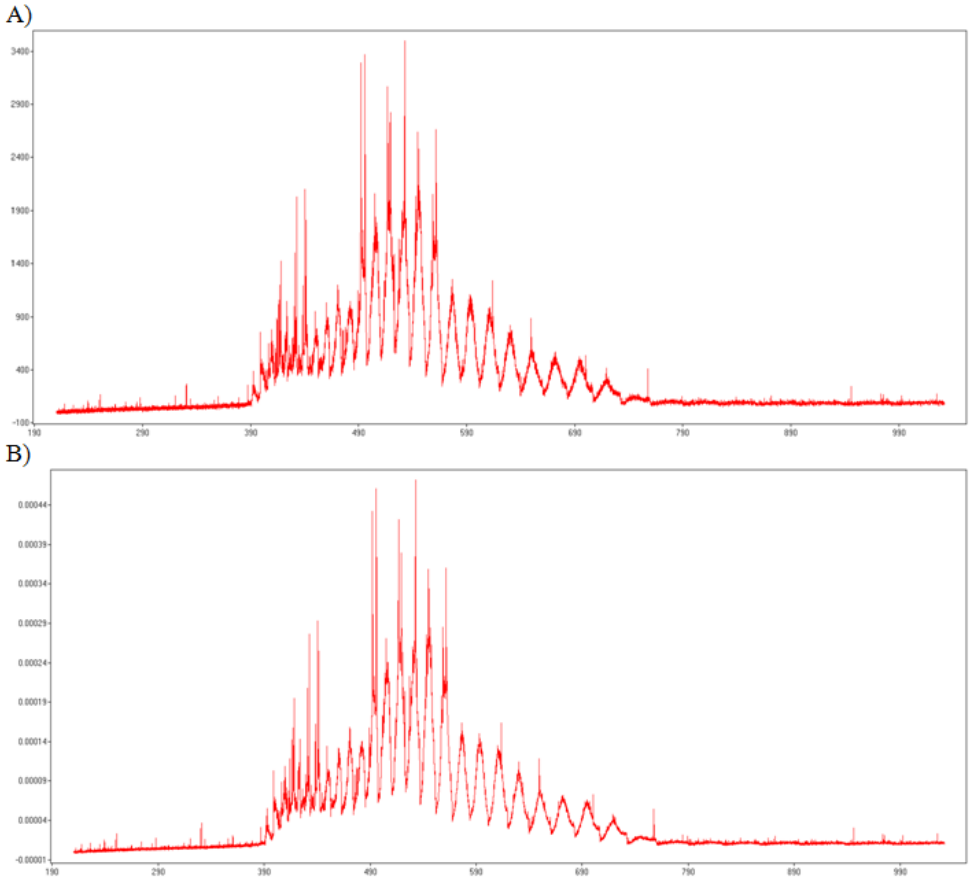

Figure 23. FeNi 90-10 spectra - (A) Un-normalized, (B) Normalized

Note that normalization of the spectrum did not result in any change in how pronounced a given emission line was relative to the rest of the spectrum. In fact, that was

the purpose of normalizing in the first place. Regardless of how bright the entire spectrum is, the proportional brightness of a given line to the rest of the spectra should be a constant across all 5 runs of the sample. The process was repeated for each of the fifteen Excel spread sheets. In each case, the data began as shown in Table 3 and was transformed to appear as in Table 4. Table 3 is a portion of the spectrum of the third run at 27kV of the FeNi 90-10 sample. Table 4 is a sample portion of the spectrum of averaged normalized counts of FeNi 90-10 at 27kV. Once the normalized averaged spectrums of each sample at each laser voltage were found, an Excel workbook of the results was created with the intention of using it to locate nickel lines.

Table 3. Example portion of imported spectrum - FeNi 90-10, 27kV, run 3

Sample	Run	Sum
FeNi 90-10	3	10939049.4
Wavelength (nm)	Counts	Normalized
471.08301	1858.15	0.000169864
471.11292	1898.75	0.000173575
471.14282	1833.32	0.000167594
471.17273	1778.73	0.000162604
471.20267	1772.18	0.000162005
471.23257	1668.83	0.000152557
471.26248	1648.1	0.000150662
471.29242	1703.78	0.000155752
471.32233	1758.94	0.000160795
471.35226	1747.6	0.000159758
471.3822	1714.27	0.000156711
471.41211	1714.99	0.000156777
471.44205	1820.74	0.000166444

Table 4. Example portion of normalized average spectrum - FeNi 90-10, 27kV

Sample	Run
FeNi 90-10 (Normalized Counts Averaged)	Null
Wavelength (nm)	Normalized Counts Averaged
471.02319	0.000170836
471.0531	0.000170793
471.08301	0.000170664
471.11292	0.00016783
471.14282	0.000163088
471.17273	0.000161954
471.20267	0.00015909
471.23257	0.000153929
471.26248	0.000155402
471.29242	0.000159134
471.32233	0.00016124
471.35226	0.000159797
471.3822	0.000160083

The workbook that was created for the purpose of locating nickel lines contained three pages; each page was for the normalized averaged spectra of a given voltage. The analysis done on each page was equivalent. Beginning with the spectral data from the FeNi 90-10 sample, the normalized averaged emission lines of the pure Fe sample was subtracted from the normalized averaged spectrum resulting from the FeNi 90-10 sample. Therefore, for every single emission across the entire spectrum of wavelengths the corresponding normalized emission of the pure Fe sample was subtracted. The motivation for doing that was that if were there any nickel emission lines in the FeNi 90-10 spectra, they would have the largest values after the difference from pure Fe was taken. The process was repeated for each normalized average spectra from each sample at each voltage, resulting tables such as Table 5.

Table 5. Normalized average spectrum of FeNi 90-10 with difference from pure Fe

Sample	Run	Sum
FeNi 90-10 (Normalized Counts Averaged)	Null	1
Wavelength (nm)	Normalized Counts Averaged	Difference
547.7486	0.000328226	8.53867E-05
547.78326	0.000303749	7.23223E-05
547.71399	0.000326137	6.95234E-05
508.10648	0.000240509	6.60693E-05
508.07425	0.000248954	6.12636E-05
471.5618	0.000187085	6.02812E-05
508.0098	0.000259233	5.98869E-05
508.1387	0.000235754	5.87349E-05
547.81787	0.000287025	5.86443E-05
507.97757	0.000270996	5.83624E-05
508.04202	0.000245424	5.82652E-05
471.53186	0.000186015	5.74724E-05
471.59174	0.000183031	5.73303E-05
507.91315	0.000267915	5.5704E-05

Table 5 shows the ability of this method to successfully find spectral lines of nickel. Looking at the wavelength column, all of the entries are remarkably close to one of three values. Those values are ~547.7nm, ~508.1nm, and ~ 471.5nm. The NIST spectral line database verifies that each one of the spectral lines belongs to nickel. Figure 24 through Figure 27 are a difference spectra for FeNi of various nickel concentrations taken at 27kV, with Ni lines labeled. The difference spectra are especially interesting because the degree to which the Ni lines are distinguished from the rest of the spectrum clearly decreases with decreasing Ni concentration in the sample. In Figure 24, the difference values corresponding to Ni emissions from the FeNi 90-10 sample are extremely distinguished, with sharp peaks protruding from the rest of the difference spectrum. Then, as shown in Figure 25 through Figure 27, the Ni difference values begin to fall into the rest of the difference spectra, becoming less pronounced with decreasing concentration in the doped samples. This relationship is exactly what was expected, and is a good indicator that Ni

emissions can be quantified in a meaningful way with respect to the rest of their host spectra.

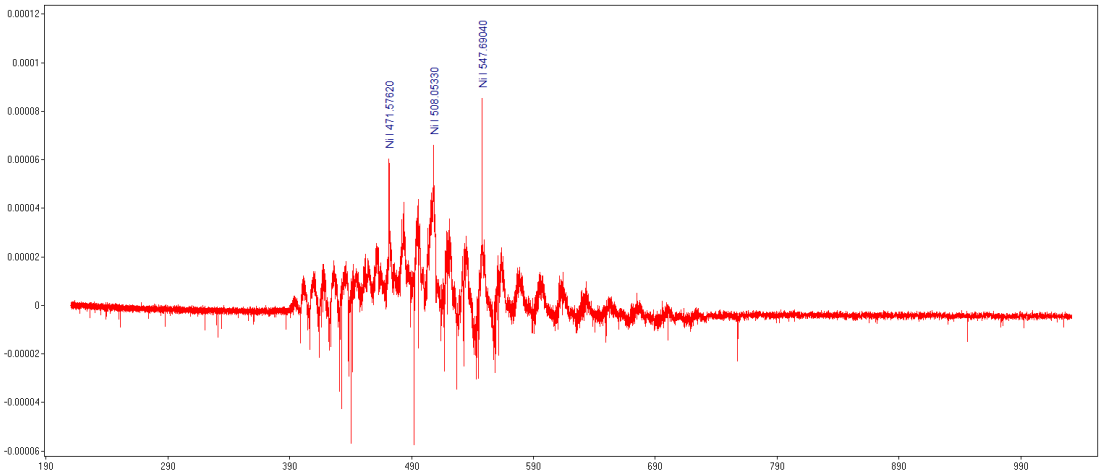

Figure 24. Difference spectrum for FeNi 90-10

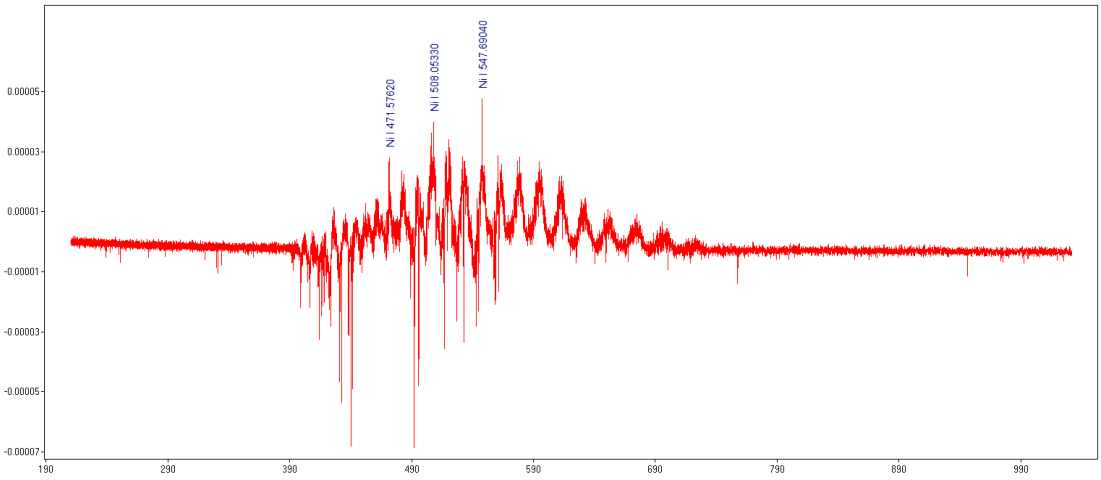

Figure 25. Difference spectrum for FeNi 95-5

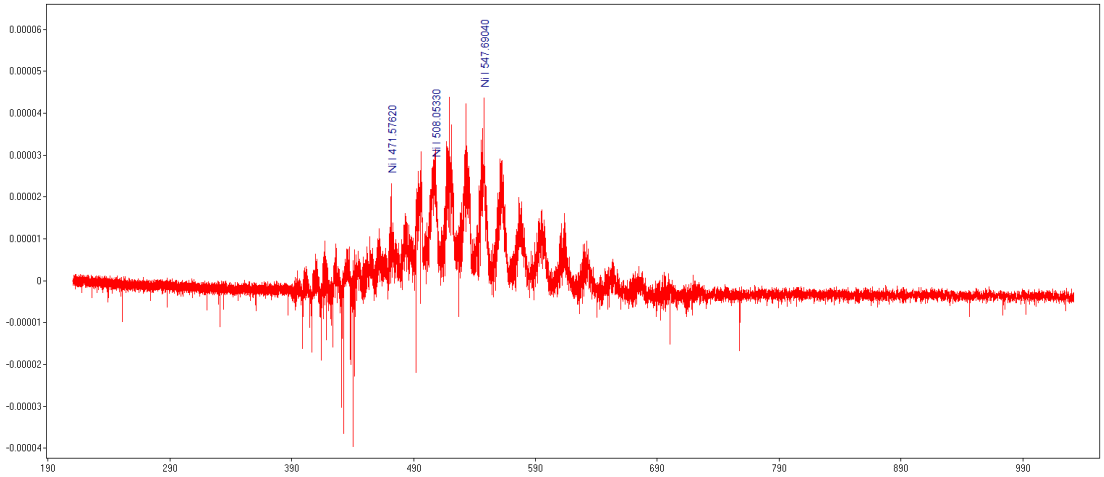

Figure 26. Difference spectrum for FeNi 98-2

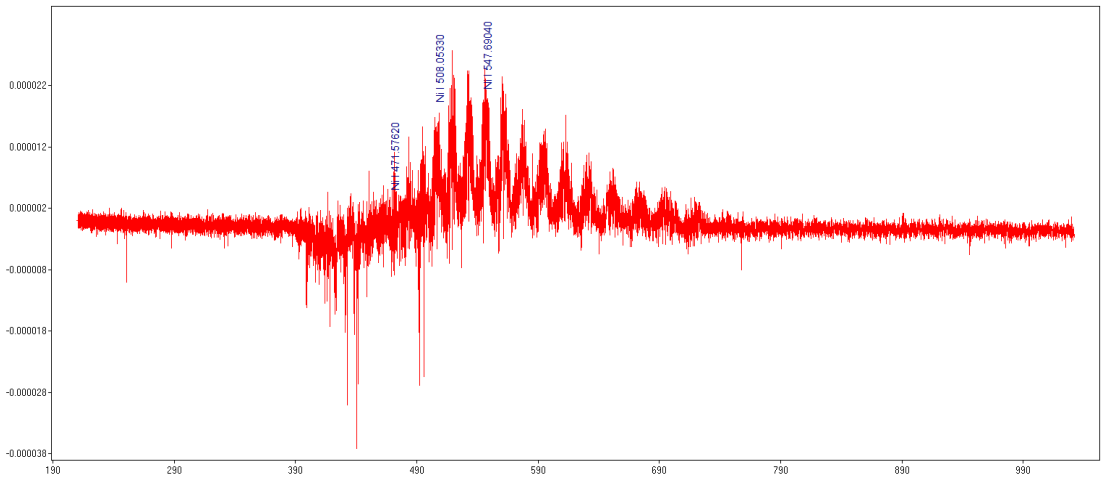

Figure 27. Difference spectrum for FeNi 99-1

After finding the locations of the nickel emission lines, it was necessary to quantify their contribution to the spectrum as a whole. Spectral lines in any given spectra are not infinitely thin because spectrometers do not have infinite precision. The gratings that split wavelengths apart in a spectrometer do not do so perfectly. There are inherent imperfections in the gratings that lead to a spread in the locations at which photons from a given emission land on the pixels of the spectrometer CCD camera. The spread results in a range in reported wavelengths for a given spectral line. The width of each emission peak of nickel appears to be the same across the normalized spectra. Therefore, the range of

wavelengths that a given nickel emission line is pronounced across is independent of the value of the wavelength it is centered upon. This is shown in Figure 28 and Figure 29.

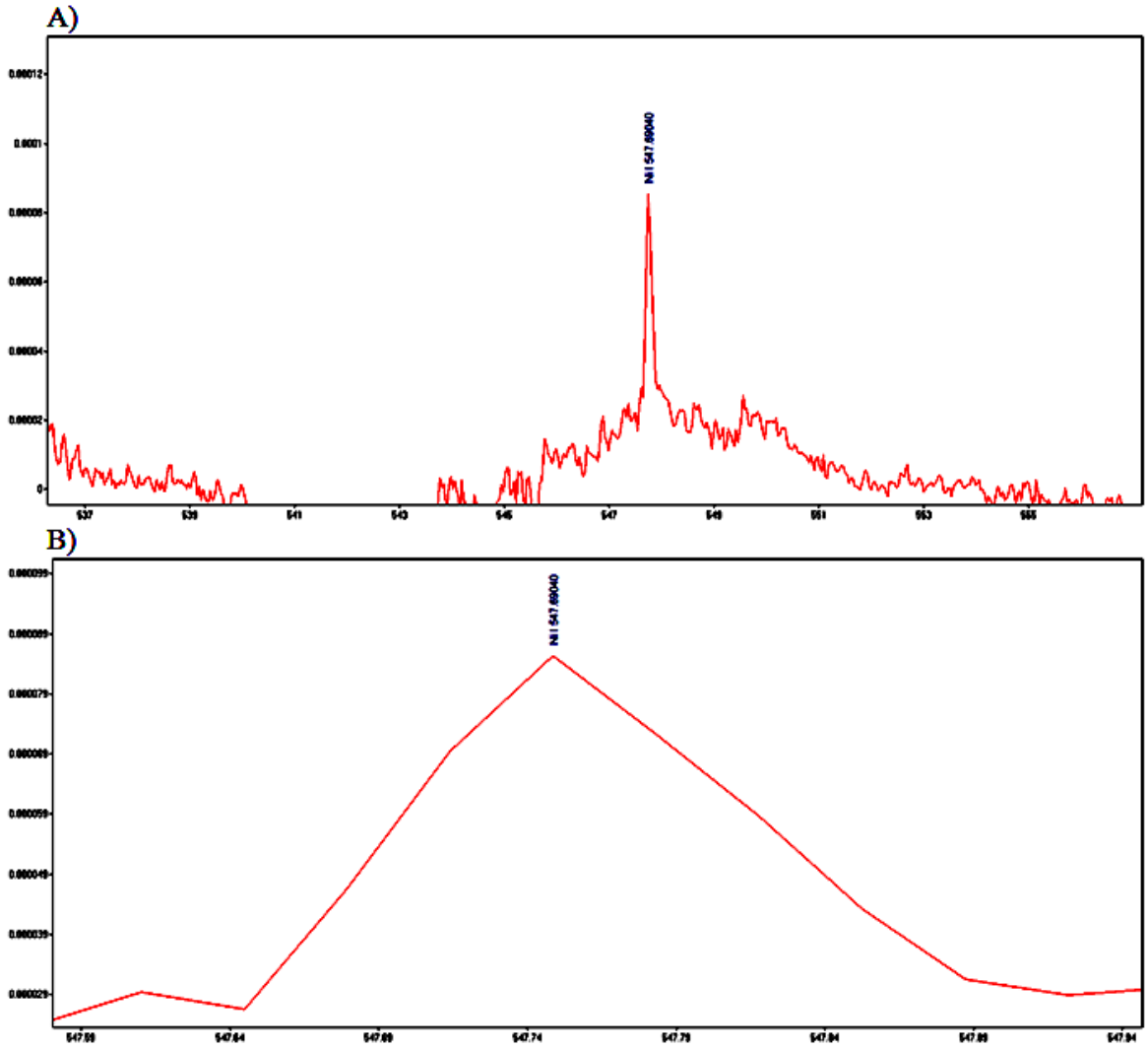

Figure 28. Normalized spectrum nearby 547.7nm

Figure 28 (A) shows a small area of the normalized FeNi 90-10 spectrum containing the 547.7nm emission line of nickel. It can be seen that there is a definite peak that stands out from the rest of the spectrum around it. Figure 28 (B) presents a much closer look at that emission peak. The peak is prominent over a ~0.3nm region. Figure 29 shows the same two perspectives around the 508.1nm emission line of nickel. While it is slightly less obvious, the region of prominence for this line is also ~0.3nm. Verification of the 471.5nm

emission line occurred and an equivalent range was found. A figure showing that result is omitted.

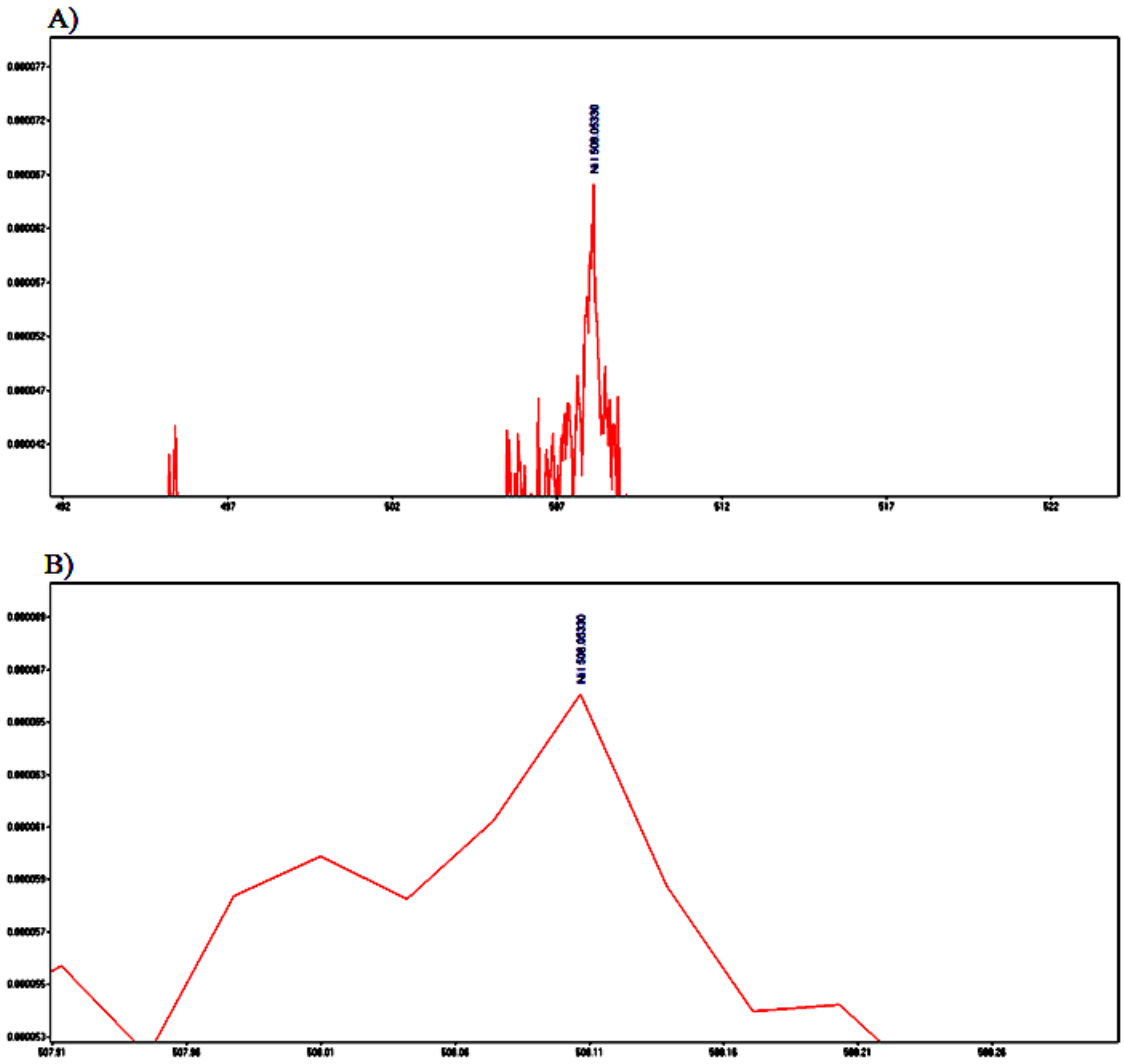

Figure 29. Normalized spectrum nearby 508.1nm

As is shown in Figure 28 and Figure 29, the range over which the emission peaks of nickel are pronounced is ~0.3nm. Therefore, one way to quantify the contribution of a nickel emission line with respect to the whole spectrum is to sum all spectral counts in a 0.3nm wavelength range around the point at which the peak of the emission is centered. That process may be repeated for the other nickel emission lines in the spectrum.

Another way to quantify the contribution of a specific line with respect to the whole spectrum is to find the average value of all the spectral counts in the 0.3nm range. This value would be the normalized counts for that specific emission *line* (italicization because this value is an average of a spread of values; the *line* is not actually measured). The two quantification methods were employed on all runs and laser voltages for all samples. The results are shown in Figure 30 and Figure 31 and their implications will now be discussed.

The six plots appearing in Figure 30 and Figure 31 show the results of the data analysis described above. The blue data points appearing in the first plot in Figure 30 represent the values of the sum of all normalized spectral counts in a 0.3nm wavelength range under the 547.7nm nickel emission line. Each blue dot comes from a single LIBS run on a given sample at laser voltage 27kV. The values are plotted against concentrations, so there are five sets of five values giving twenty-five values in total. The sum of normalized spectral counts for each run was averaged in order to find a representative value for the sums of normalized spectral counts and the result was plotted along with the individual runs. This was repeated for each concentration, yielding average values for the sum of normalized spectral counts over the 0.3nm wavelength range around 547.7nm. Using the average values, a trend line was constructed to act as the calibration curve for that emission. The process was repeated for the 508.1nm emission line (red data points) and the 471.5nm emission line (green data points). The process just described was used to create the data from the 25kV laser voltage runs as well as the 23kV laser voltage runs (Figure 30, 2nd and 3rd plots).

The graphs appearing in Figure 31 were similarly constructed. The blue data points in the first plot in Figure 31 represent the average of all spectral counts in the 0.3nm range

around the 547.7nm emission line taken at laser voltage 27kV, and are plotted against concentration. As previously stated, the value of these data points can be considered as the calculated normalized emission *line* for that spectral emission. The emission *lines* were then averaged together to find a representative value for the 547.7nm emission line at a given concentration. The process was repeated for all concentrations and resultant values were plotted along with those from the individual runs. An equivalent process was used for the 508.1nm (red data points) emission line and the 471.5nm emission line (green data points). Trend lines were then applied to the resultant data, giving calibration curves for the spectral emissions. The 2^{nd} and 3^{rd} plots in Figure 31 correspond to the 25kV laser voltage runs and the 23kV laser voltage runs, respectively.

Figure 30 and Figure 31 represent the contribution of a given emission line to the spectrum as a whole. It is clear from the results that the contribution of a dopant spectral emission lines to the spectrum as a whole increases with concentration. That relationship appears to be linear. However, more research into this topic along with an independent replication of the work should be pursued to verify the results.

Based on the data, it may be that the FeNi 95-5 sample has a manufacturing error. Looking at the results in Figure 30 and Figure 31, the contribution of nickel to the spectrum appears low. In fact, in certain runs its contribution is smaller than the FeNi 98-2 sample. The measurements on the FeNi 95-5 sample were repeated and the entirety of the data analysis process was also repeated to eliminate any accidental errors but very similar results were found. Therefore, a new FeNi 95-5 sample should be ordered and tested. Once that has been done, the data analysis described should be repeated and the results spliced in. Then the predictability of the newly found calibration curve should be tested.

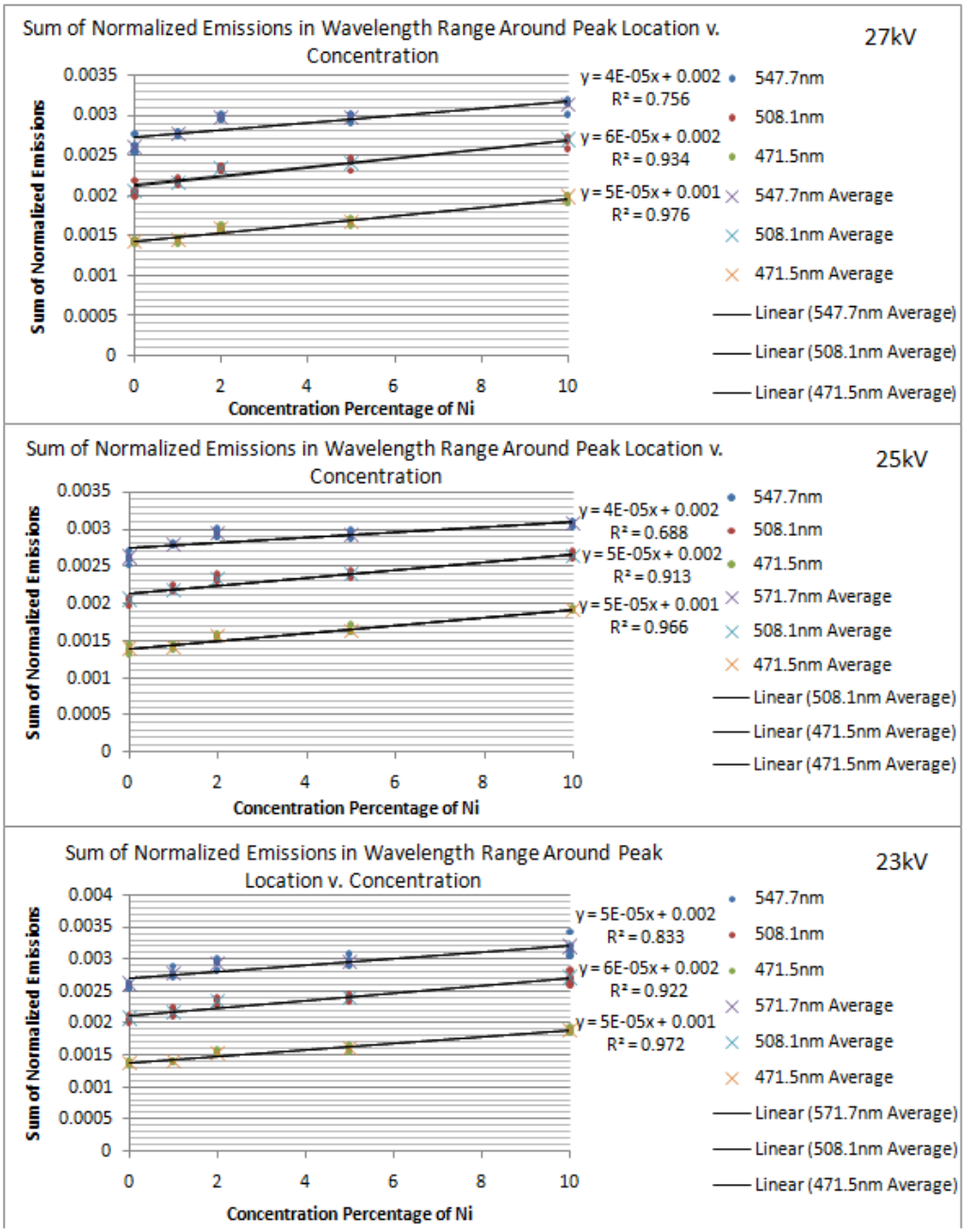

Figure 30. Calibration curve for sums

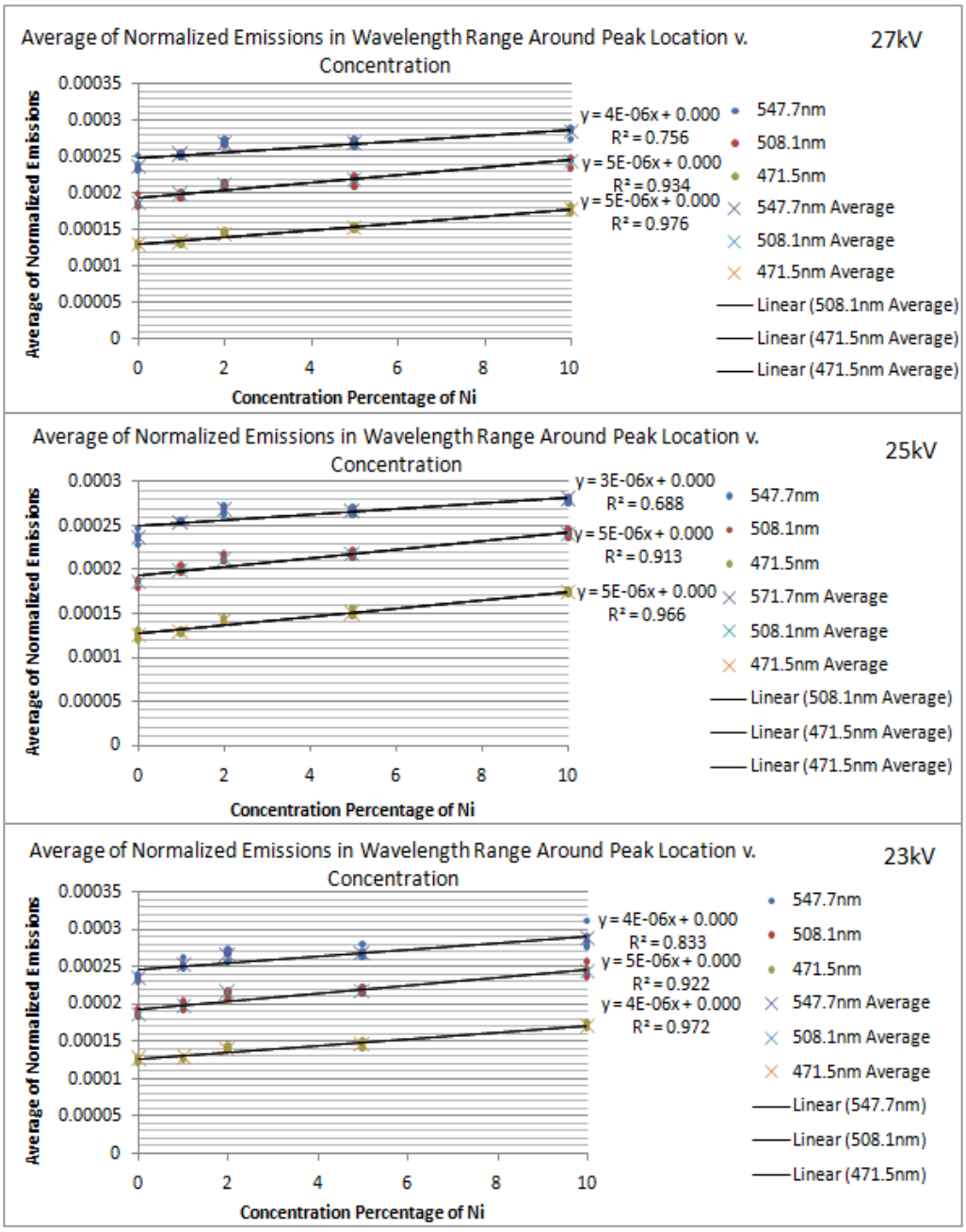

Figure 31. Calibration curve for averages

Future Work

It is highly likely that there are other Ni lines that were not found. It would be beneficial if future graduate students could do a more comprehensive analysis on the data to seek out all nickel lines. Hopefully the analysis will include the negative difference lines

in the above spectra. The negative difference lines correspond to elements residing within the pure Fe sample that did not exist within the nickel-doped Fe samples. It may be noted that the pure Fe sample had rust splotches. Therefore, the negative difference lines may be from oxygen spectral emissions.

While LIBS is a minimally-invasive method for doing materials analysis, it does require superficial ablation of the working sample. Micro-LIBS is an area of research focused on achieving reliable spectroscopic measurements while only ablating areas on the order of microns in diameter. A major issue with micro-LIBS is that the amount of light emitting from the plasma plume is proportional to the size of the plume itself. The fiber optics of spectrometers are highly sensitive to adjustment and thus must be in exactly the right position. Any deviation from the correct position will result in too little light to be delivered by the fiber optics to the internal spectrometer optics to obtain accurate and informative spectra. Having minimal plume emission will only amplify that problem. With the right instrumentation, it is possible to build an optical path with a configuration capable of creating micron size craters while allowing for good spectroscopy. That should be a research project for future graduate students.

There are numerous variables that affect the results of LIBS. Environmental factors such as room temperature, air pressure, and humidity need to be controlled in order to produce the best and most consistent data possible. One solution is to do LIBS in a vacuum. Pulsed laser deposition of thin films has previously been achieved at UMKC. With the single-objective design of the optical path, it is possible to place the spectrometer outside of the vacuum chamber, allowing for both thin films research and LIBS to be conducted with the same optical path.

The spectroscopic results are also highly dependent on how well ablation occurs, and thus how focused the laser is on the sample. With a high power objective, minor adjustments to the position of the sample result in significant changes in the spectra obtained. Additional consideration should be given to the design of the sample holder so that it is somehow affixed to the main objective. The sample holder itself should be dynamic enough to allow for variability in the size and shape of the sample, while also being immune to any unwanted large-scale adjustments.

The amount of ablation also depends on the power of the laser itself. Small changes in laser power can produce significant changes in the brightness of spectral lines. A power meter should be added to the optical path and effort should be spent on keeping the power a constant.

Repeatability and the ability to predict results are crucial in science. Future students should use the results of this research as a launch point for further studies on relating spectral line intensity. If the variables aforementioned in this section are kept constant it is very likely that the individual doing the research will find the desired results.

In the present analysis, normalized spectral counts over a 0.3nm wavelength range were considered to be representative of the contribution of a given emission line. There are better ways of quantifying the contribution of an emission line to the rest of the spectrum. Future research effort should be focused on finding a way to determine the full-width half-max of a given emission line. Doing so would allow a more accurate determination of the contribution of an emission line to the spectrum.

The data analysis presented in this thesis is not unique to nickel. It is hoped that future students will repeat this process on other multi-element samples and that the results will be useful and accurate.

CHAPTER 4

CONCLUSION

In this thesis I have discussed in detail all of the endeavors required to construct calibration curves for determining the concentrations of nickel in nickel-doped samples of iron. A suitable configuration for the internal resonator optics of the excimer laser was found. The configuration is known as the unstable resonator configuration and it produces a flat-top laser beam profile. The flat-top beam profile was preferable to the Gaussian profile which could not be resolved into a single ablation spot.

Once the laser was emitting a beam that could be focused desirably, an optical path was designed that would be applicable to both LIBS and microLIBS. The optical path was equipped with a sample visualization segment that was activated by a flip-mirror. When in visualization mode the sample could be accurately positioned for aiming at particles on the order of microns.

The optical path was used for LIBS on iron samples doped with nickel at various concentrations. Through rigorous data analysis a procedure was developed for locating spectral emission lines from nickel. Three nickel emissions were located and the contributions to their host spectra were quantified. The results were plotted against concentration, culminating in calibration curves for FeNi samples.

The data analysis developed in this thesis is not unique in any way to nickel. It is important to note that this process could have been done on any multi-element material.

REFERENCES

[1] C. Pasquini, J. Cortez, L. Silva, and F.B. Gonzaga, J. Braz. Chem. Soc. **18**, 463 (2007).

[2] F. Anabitarte, A. Cobo, and J.M. Lopez-Higuera, ISRN Spectrosc. **2012**, 1 (2012).

[3] F.B. Gonzaga, W.F. de C. Rocha, and D.N. Correa, Spectrochim. Acta Part B At. Spectrosc. **109**, 24 (2015).

[4] G. Bilge, H.M. Velioglu, B. Sezer, K.E. Eseller, and I.H. Boyaci, Meat Sci. **119**, 118 (2016).

[5] L.M. Cabalín, A. González, J. Ruiz, and J.J. Laserna, Spectrochim. Acta Part B At. Spectrosc. **65**, 680 (2010).

[6] Y. Wang, H. Yuan, Y. Fu, and Z. Wang, Spectrochim. Acta Part B At. Spectrosc. **126**, 44 (2016).

[7] E.C. Ferreira, D.M.B.P. Milori, E.J. Ferreira, R.M. Da Silva, and L. Martin-Neto, Spectrochim. Acta Part B At. Spectrosc. **63**, 1216 (2008).

[8] Y.G. Mbesse Kongbonga, H. Ghalila, M.B. Onana, and Z. Ben Lakhdar, Food Chem. **147**, 327 (2014).

[9] J. Singh, R. Kumar, S. Awasthi, V. Singh, and A.K. Rai, Food Chem. **221**, 1778 (2017).

[10] S. Moncayo, S. Manzoor, J.D. Rosales, J. Anzano, and J.O. Caceres, Food Chem. **232**, 322 (2017).

[11] M.P. Casado-Gavalda, Y. Dixit, D. Geulen, R. Cama-Moncunill, X. Cama-Moncunill, M. Markiewicz-Keszycka, P.J. Cullen, and C. Sullivan, Talanta **169**, 123 (2017).

[12] H. Wiggenhauser, D. Schaurich, and G. Wilsch, Ndt E Int. **31**, 307 (1998).

[13] F. Sorrentino, G. Carelli, F. Francesconi, M. Francesconi, P. Marsili, G. Cristoforetti, S. Legnaioli, V. Palleschi, and E. Tognoni, Spectrochim. Acta Part B At. Spectrosc. **64**, 1068 (2009).

[14] X. Cama-Moncunill, M. Markiewicz-Keszycka, Y. Dixit, R. Cama-Moncunill, M.P. Casado-Gavalda, P.J. Cullen, and C. Sullivan, Food Control **78**, 304 (2017).

[15] M. Markiewicz-Keszycka, X. Cama-Moncunill, M.P. Casado-Gavalda, Y. Dixit, R. Cama-Moncunill, P.J. Cullen, and C. Sullivan, Trends Food Sci. Technol. **65**, 80 (2017).

[16] L. Zheng, F. Cao, J. Xiu, X. Bai, V. Motto-Ros, N. Gilon, H. Zeng, and J. Yu, Spectrochim. Acta Part B At. Spectrosc. **99**, 1 (2014).

[17] X. Yang, Z. Hao, M. shen, R. Yi, J. Li, H. Yu, L. Guo, X. Li, X. Zeng, and Y. Lu, Talanta **163**, 127 (2017).

[18] J. Li, L. Guo, N. Zhao, X. Yang, R. Yi, K. Li, Q. Zeng, X. Li, X. Zeng, and Y. Lu, Talanta **151**, 234 (2016).

[19] C. Suplee, NIST (2009).

[20] O.R. Musaev, A.E. Midgley, J.M. Wrobel, and M.B. Kruger, Chem. Phys. Lett. **487**, 81 (2010).

[21] J.M. Wrobel, *Final Report for Honeywell* (University of Missouri - Kansas City, 2017).

[22] Z. Navrátil, D. Trunec, R. Šmíd, and L. Lazar, Czechoslov. J. Phys. **56**, 944 (2006).

VITA

Jesi Claire Polaris was born in Tulsa, Oklahoma on January 5, 1992. She was educated in the Union public school system, graduating from there in May 2010. She graduated from The University of Tulsa in May 2015 with a Bachelor of Science degree in Mathematics and Physics, completing a thesis on the behavior of timelike and lightlike geodesics in various space-time geometries. She completed the University of Tulsa Summer Undergraduate Research Program in Physics (SURPP), where the focus of her research was the geometric optimization of microring resonators. She held two separate officer positions in The University of Tulsa chapter of the Society of Physics Students (∑∏∑).

In January 2016, Ms. Polaris began the Masters of Physics program at the University of Missouri – Kansas City, where the focus of her research was laser induced breakdown spectroscopy. She has held both Graduate Teaching Assistant and Graduate Research Assistant positions at the University of Missouri – Kansas City.